Journal of Materials Chemistry A

PAPER

Check for updates

Reducing the confinement of PBDB-T to ITIC to improve the crystallinity of PBDB-T/ITIC blends†

Qiuju Liang,[ab] Jie Han,[c] Chunpeng Song,[c] Xinhong Yu,[a] Detlef-M. Smilgies, [iD][d] Kui Zhao,*[e] Jiangang Liu*[a] and Yanchun Han [iD] *[a]

The ordered aggregation of non-fullerene small molecular acceptors (SMAs) plays a key role in determining the charge transport and bimolecular recombination in polymer/SMA solar cells. However, due to the competition between crystallization and phase separation, the polymers are prone to form a network first, which inhibits the molecular diffusion of SMAs, resulting in weak crystallinity of SMAs. Here, we demonstrated a sequential crystallization method for high performance PBDB-T/ITIC solar cells with much improved crystallinity of ITIC. By tuning the sequence of thermal annealing (TA) and solvent vapor annealing (SVA), sequential crystallization of ITIC and PBDB-T can be fine controlled to grow a highly crystalline ITIC and PBDB-T network. The crystallization kinetics results indicate that when the crystallization of ITIC occurred prior to the formation of the PBDB-T crystallized network, the crystallinity of ITIC is significantly improved due to high molecular diffusion. However, if the crystallization of PBDB-T occurred first, the diffusion of ITIC was restricted by the crystalline network of PBDB-T, resulting in a low crystallinity of ITIC. The enhanced crystallinity of ITIC is beneficial to the electron transport and suppressed the bimolecular recombination, which helps boost the device performance from 8.14% to 10.95%. This work demonstrates that manipulation of the crystallization sequence of the donor and acceptor may be key to further boost the efficiency of polymer/SMA solar cells.

Introduction

Organic solar cells (OSCs) based on solution-processed bulk heterojunctions (BHJs) have attracted considerable attention over the past few decades due to their solution processability, low cost, light weight, and flexibility.[1–3] Although both fullerene and non-fullerene small molecular acceptors (SMAs) are extensively employed in BHJ OSCs, SMAs potentially have great advantages in highly tunable molecular energy levels, light absorption spectra, and low voltage loss compared to their fullerene counterparts.[4–6] Due to the rapid development of novel SMAs, the impressive power conversion efficiencies (PCEs) of OSCs have surpassed 14%.[7–9]

In addition to synthesis of ideal SMAs, morphology is also of critical importance to the device performance.[10,11] It has been demonstrated that the ideal morphology of active layer should involve a highly crystalline and interconnected network of phase-separated domains with large donor/acceptor interfacial areas.[12,13] The domain size should be comparable to the exciton diffusion length for efficient free carrier generation and the intermolecular π–π interactions of both components must be strong to ensure carrier transport.[14,15] Unfortunately, in order to meet the requirement of domain size, the ordered stacking of SMAs is usually sacrificed in polymer/SMA blend systems. As a result, the electron mobilities in many high-efficiency non-fullerene-based OSCs were less than 10^{-4} cm^2 V^{-1} s^{-1}, *i.e.* one or two orders of magnitude lower than that in fullerene-based OSCs, leading to increased bimolecular recombination.[6] Hou *et al.* proposed that enhancing the ordered aggregation, especially the crystallinity of the acceptor in polymer/SMA blend systems, could significantly improve the electron mobility and diminish charge recombination. In addition, a positive correlation was also found between the crystallinity of SMAs with the device fill factor (FF) and photocurrent density (J_{SC}), which further indicated the importance of ordered stacking of SMAs for state-of-art high-efficiency non-fullerene OSCs.[16,17]

However, enhancing the crystallinity of SMAs is not a simple task in polymer/SMA blend systems, since the polymer tends to inhibit the aggregation of SMAs.[18] Due to the large difference of

[a]State Key Laboratory of Polymer Physics and Chemistry, Changchun Institute of Applied Chemistry, Chinese Academy of Sciences, Changchun 130022, P. R. China. E-mail: niitawh@ciac.ac.cn; ychan@ciac.ac.cn

[b]University of the Chinese Academy of Sciences, Beijing 100049, P. R. China

[c]State Key Laboratory of High Power Semiconductor Lasers, Changchun University of Science and Technology, Changchun 130022, P. R. China

[d]Cornell High Energy Synchrotron Source, Cornell University, Ithaca, NY 14850, USA

[e]Key Laboratory of Applied Surface and Colloid Chemistry, National Ministry of Education, Shaanxi Key Laboratory for Advanced Energy Devices, Shaanxi Engineering Lab for Advanced Energy Technology, School of Materials Science and Engineering, Shaanxi Normal University, Xi'an 710119, P. R. China. E-mail: zhaok@snnu.edu.cn

† Electronic supplementary information (ESI) available. See DOI: 10.1039/c8ta05892j

molecular weights, the phase separation kinetics in polymer/ SMA blend systems is usually asymmetric.[19] As the polymer component relaxes much slower than the concentration growth during the film formation or post-annealing process, it would induce an internal network stress. As a result, the polymer in the blend, even if the content is extremely low, is able to form interconnected phase domains and network-like structures.[20] The preformed polymer network would block the diffusion of SMAs, which would further inhibit the crystal growth of SMAs. In light of the above reasons, SMAs tend to be amorphous or form crystals with small size in polymer/SMA blend systems.

Molecular tailoring, *i.e.*, reducing the steric hindrance or enhancing the π–π interaction, is an effective way to increase the ordered molecular packing of SMAs. Holliday *et al.* used the linear group (*n*-octyl) to substitute the branched group (2-ethylhexyl), which reduced the steric hindrance of IDTBR, leading to a great increase in molecular crystallinity.[21] Zhan *et al.* replaced the phenyl side-chains of ITIC with 2-thienyl groups, causing an enhanced π–π interaction and also leading increased crystallinity.[22] In addition, the crystallinity of SMAs could be enhanced by lowering the miscibility between the polymer and SMAs as well.[23,24] The Flory–Huggins interaction parameter (χ) is known as a fundamental metric of the degree of mixing, the relatively higher χ parameter is in agreement with the lower degree of mixing.[25] Hou *et al.* increased the χ parameter in PBDB-TF/SMA blend system 15-fold by strengthening the intramolecular electron push–pull effect of SMAs. The increased χ parameter lowers the miscibility between PBDB-TF and SMAs, which is beneficial to achieve higher crystallinity and domain purity. Hence, higher carrier mobility and lower bimolecular recombination were achieved.[23]

Physicists always want to find some easy ways to enhance the aggregation of SMAs in polymer/SMA blend systems. The traditional methods, such as thermal annealing (TA),[26] solvent vapor annealing (SVA)[27,28] and using a solvent additive,[29] are effective in polymer/fullerene blend systems, and have been executed to control the morphology of polymer/SMA blend systems as well.[30,31] While all these methods could enhance the crystallinity of the polymer, they have little effect on the aggregation of SMAs. Obviously, although these achievements illustrate a significant breakthrough in device performance *via* material design, many essential problems are yet to be solved: What is the principle to enhance the ordered aggregation of SMAs in polymer/SMA blend systems? How can the final crystallization morphology be controlled *via* thermodynamics or kinetics?

Here, we systematically investigated influence of the sequential crystallization of PBDB-T/ITIC blends on the crystallinity of both components. A two-step annealing approach, including solvent vapor annealing (SVA) and thermal annealing (TA), was employed to control the crystallization sequence. SVA is employed to selectively improve the crystallinity of ITIC by choosing tetrahydrofuran (THF) as solvent vapor, since it has a much higher solubility for ITIC than for PBDB-T. The crystallinity of PBDB-T was increased at the TA temperature of 150 °C because the crystallization of PBDB-T and ITIC is above 120 °C and 180 °C, respectively. As a result, the sequential

crystallization was realized by the tuning the order of SVA and TA treatment. Our results show that the prior crystallization of ITIC without the confinement of the PBDB-T crystallized network can significantly enhance the crystallinity of ITIC compared to the prior crystallization of PBDB-T due to high molecular diffusion. The enhanced crystallinity of ITIC is beneficial for the formation of pure phases and inter-penetrating networks, which increases electron mobility and reduces bimolecular recombination. Thus, the device performance was improved from 8.14% to 10.95%.

Experimental section

Materials

Poly[(2,6-(4,8-bis(5-(2-ethylhexyl)thiophen-2-yl)benzo[1,2-*b*:4,5-*b′*]-dithiophene)-*co*-(1,3-di(5-thiophen-2-yl)-5,7-bis(2-ethylhexyl) benzo[1′,2′-*c*:4,5-*c′*]dithiophene-4,8-dione))] (PBDB-T, M_n = 78 kDa, PDI = 2.1) and 3,9-bis(2-methylene-(3-(1,1-dicyano-methylene)-indanone))-5,5,11,11-tetrakis(4-hexylphenyl)-dithieno [2,3-*d*:2′,3′-*d′*]-*s*-indaceno[1,2-*b*:5,6-*b′*]dithiophene) (ITIC) were purchased from Solarmer Materials Inc. The structure and energy level of which are shown in Scheme 1. Chlorobenzene (CB), zinc acetate, ethylene glycol monomethyl ether and ethanolamine were purchased from Sigma-Aldrich. Tetrahydrofuran (THF) was purchased from Beijing Chemical Factory, China. The materials were used as received.

Thermal annealing

PBDB-T/ITIC (total concentration of 20 mg mL^{-1} with PBDB-T/ ITIC weight ratio of 1 : 1) chlorobenzene solution was stirred at 100 rpm and heated for 12 h. Subsequently, the solution was kept at room temperature for around 1 h. Then, the solution was spin-coated at 3000 rpm for 30 s to obtain pristine films. The thermal annealing process is the heating of films at 150 °C for 30 min.

The solvent vapor annealing

The film was placed in a glass tube which contained THF at the bottom. The stable vapor gradient can be obtained at around 20 min since the THF location was fixed. The vapor pressure around the sample was $P = 0.54$ (25 °C) (The total tube length is 3 cm and the liquid height is 0.2 cm. The solvent vapor pressure P is defined as $P = L/L_0$, where L is the distance from the upper edge of the setup to the position of the specimen and L_0 is the distance from the upper edge of the setup to the surface of the solvent at the bottom of the tube). All the processes were operated in a N$_2$-filled glovebox.

Characterization

The photon absorption spectra of the active layer were recorded using a UV-vis absorption spectrometer (AvaLight-Hal) with halogen lamp source.

The fluorescence spectra of films were obtained using an Edinburgh fluorescence spectrometer (FLSP920).

The AFM images were obtained using a Veeco Instruments Nanoscope in tapping mode. A silicon microcantilever was used
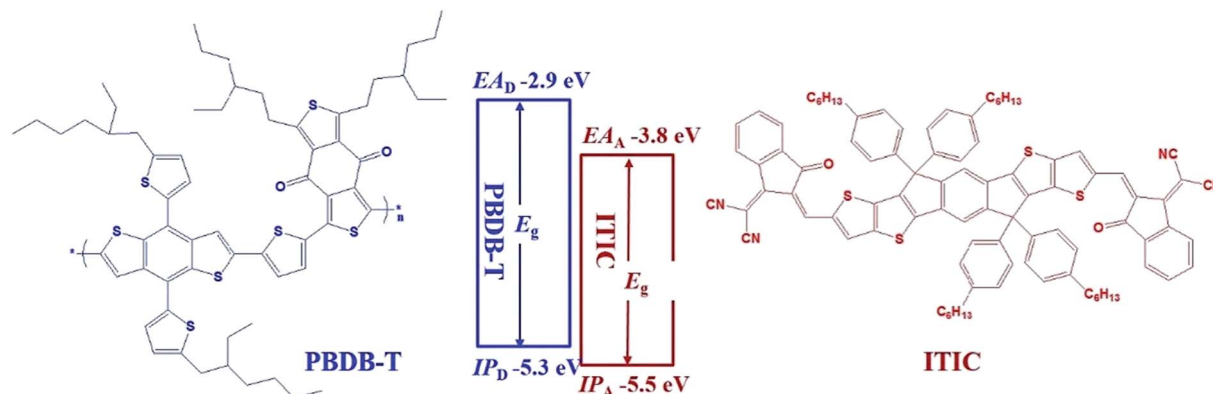
Scheme 1 The chemical structures and energy levels of PBDB-T and ITIC.

for the scanning with a spring constant of 2 N m^{-1} (resonant frequency $\approx$ 70 kHz, Olympus, Japan).

The crystallinity of the films was characterized using grazing incidence wide angle X-ray scattering (GIWAXS) measurements at the D-line of the Cornell High Energy Synchrotron Source (CHESS). The wavelength of the X-ray was 1.162 Å and the bandwidth $\Delta\lambda/\lambda$ was 1.5%. The scattering signal was monitored using a Pilatus 200K detector, the pixel size of which is 172 μm by 172 μm and is placed 173.455 mm away from the sample position. The incidence angle of the X-ray beam was 0.3°.

PSC device fabrication and testing

The thin film solar cells were fabricated with the structure of indium tin oxide (ITO)/ZnO/PBDB-T:ITIC/MoO$_3$/Al. The ITO glass substrates were cleaned with detergent, deionized water, acetone, and isopropanol under sonication for 20 min, respectively, and dried by nitrogen flow. Subsequently, the ZnO layer was spin-coated on the top of the UV-ozone treated ITO glass substrate and dried at 200 °C for 60 min. A solution with PBDB-T/ITIC 10 mg/10 mg mL^{-1} CB was spin-coated on the substrate to obtain the active layer. Finally, the device was completed by a bilayer structure of MoO$_3$ (10 nm)/Al (100 nm) on top of the active layer through thermal evaporation under a vacuum of 2×10^{-4} Pa. Four solar cells, each with an active area of 7.2 mm^2, were fabricated per ITO glass substrate.

The current density–voltage (J–V) curves of the organic solar cells were measured under AM1.5G illumination at 100 mW cm^{-2} from a calibrated solar simulator using a computer controlled Keithley 236 source meter. The external quantum efficiency (EQE) data of the device were obtained using a QE-R3011 (Enli Technology Co., Ltd.) and the monochromatic light was obtained from a xenon lamp.

SCLC device fabrication and measurement

The hole and electron mobilities of PBDB-T/ITIC blend films treated with different TA and SVA orders were measured by the space-charge-limited current (SCLC) method.[32] The hole-only and electron-only device structures are ITO/PEDOT:PSS (40 nm)/active layer/MoO$_3$ (10 nm)/AL (100 nm) and ZnO/active layer/PFNBr/Al (100 nm), respectively. The current–

voltage (J–V) curves in the range of 0–5 V were recorded using a computer controlled Keithley 2400 source meter, and the results were fitted with a space charge limited function (1):

$$J = \frac{9}{8}\varepsilon_r\varepsilon_0\mu\frac{V^2}{L^3}\exp\left(0.89\beta\frac{\sqrt{V}}{\sqrt{L}}\right) \qquad (1)$$

where J is the current density, ε_0 is the permittivity of the free space, ε_r is the relative permittivity (ε_r is assumed to be 3 for the polymers), μ is the zero-field mobility, V is the potential across the device ($V = V_{applied} - V_{bi} - V_{series}$), L is the thickness of active layer, and β is the field-activation factor. The series and contact resistance (V_{series}) of the device (10–15 Ω) were measured using the blank device of ITO/PEDOT:PSS/MoO$_3$/Ag.

Results and discussion

Here, we demonstrated a sequential crystallization realized by tuning the sequence of thermal annealing (TA) and selective solvent vapor annealing (SVA) fine controlling the crystallization and phase separation for ITIC and PBDB-T. We found that the prior crystallization of ITIC to the crystallization of PBDB-T is beneficial for increasing the crystallinity of ITIC in PBDB-T/ITIC blends. The increased crystallinity of ITIC facilitated the formation of an interpenetrating network, causing an enhanced device performance.

The independent control of the crystallinity of ITIC and PBDB-T

Different kinds of molecules generally have different crystallization temperatures due to the different molecular properties. The XRD diffraction peaks located at around 22.5° and around 4.5° correspond to the (010) plane of ITIC and the (100) plane of PBDB-T, respectively (Fig. S1†). Fig. 1(A) shows the corresponding XRD diffraction peak intensity against the annealing temperature. It is obvious that the temperature which triggered the crystallization for PBDB-T and ITIC during the TA process is above 120 °C and 180 °C, respectively. Although the crystallinity of PBDB-T and ITIC can be improved when the TA temperature increases over 180 °C, the phase separation structure is destroyed (the film morphology after TA at different temperatures is shown

15612 | J. Mater. Chem. A, 2018, 6, 15610–15620

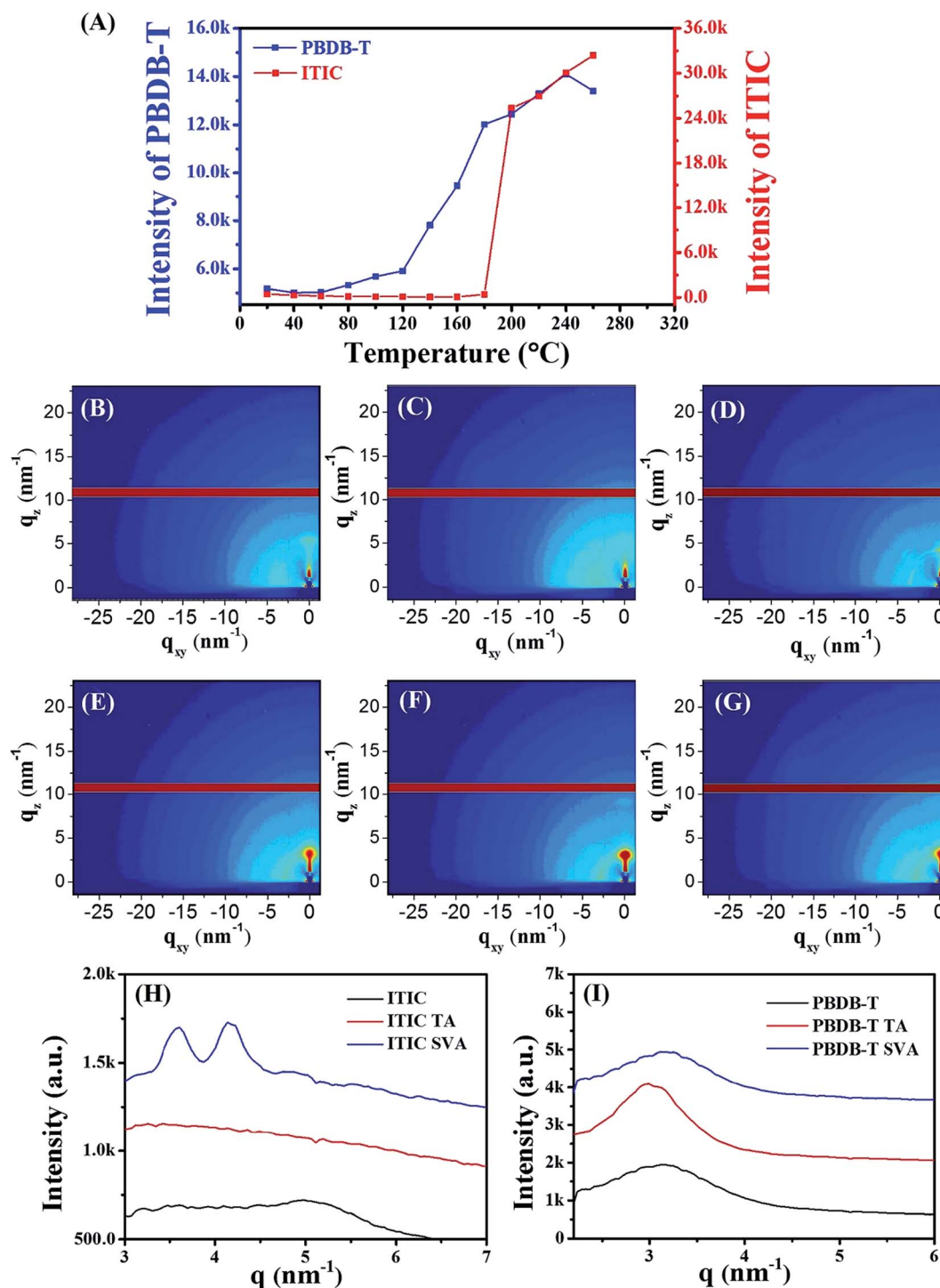This journal is © The Royal Society of Chemistry 2018

Fig. 1 (A) The variation of XRD diffraction intensity with TA temperature. The GIWAXS diffraction profiles of ITIC without annealing (B), TA at 150 °C for 30 min (C) and with THF SVA (D). The GIWAXS diffraction profiles of PBDB-T without annealing (E), TA at 150 °C for 30 min (F) and with THF SVA (G). The intensity vs. q for the diffraction features for ITIC without and with different annealing methods (H), and for PBDB-T without and with different annealing methods (I).

in Fig. S2†). Hence, we chose 150 °C as the TA temperature in this work unless otherwise stated.

Grazing-incidence wide angle X-ray scattering (GIWAXS) was carried out to monitor the variation of the crystallinity of the neat ITIC and PBDB-T films as shown in Fig. 1(B)–(G), with the

corresponding intensity vs. q for the diffraction features presented in Fig. 1(H) and (I). The pristine ITIC film shows a weak diffraction peak located at 5.0 nm^{-1} (Fig. 1(B)), indicating a low crystallinity, which can be attributed to the steric hindrance of tetrahexylphenyl substituents. The TA treatment does not

improve the crystallinity of ITIC as shown in Fig. 1(C). The PBDB-T film displays well-ordered (100) lamellar diffraction features at $q = 3.1$ nm^{-1} as shown in Fig. 1(E), which means a strong crystallinity of PBDB-T.[33] After the TA treatment, the corresponding diffraction intensity becomes stronger (Fig. 1(F)), indicating an enhanced crystallinity of PBDB-T. We can draw the conclusion that TA at 150 °C is an effective method to selectively enhance the crystallinity of PBDB-T, which also works in the PBDB-T/ITIC blend system as shown in Fig. S3(B) and (D).†

It is well known that the precondition of crystallization is mass transport and rearrangement.[34] THF is a selective solvent for PBDB-T/ITIC blends, which can dissolve ITIC and PBDB-T over 50 and less than 0.5 mg mL^{-1}, respectively. Hence, THF SVA could independently control the crystallinity of ITIC. The SVA time is selected as 30 s unless otherwise stated because the morphology of the film shows obvious phase boundaries as shown in Fig. S4.† As shown in Fig. 1(D), the ITIC film with SVA shows a stronger diffraction peak at around 5.0 nm^{-1}, and additional peaks at 3.5 nm^{-1} and 4.2 nm^{-1}. This observation indicates an enhanced crystallinity and more complicated crystalline texture.[35] However, the diffraction signal of PBDB-T remains almost unchanged (Fig. 1(G)). Because THF vapor cannot promote the movement of PBDB-T due to the low solubility, there is negligible influence of SVA on the crystallinity of PBDB-T. These observations suggest that the THF vapor treatment could selectively enhance the crystallinity of ITIC, which also works in the PBDB-T/ITIC blend system as shown in Fig. S3(C) and (D).† The independent control of the crystallinity of ITIC and PBDB-T was further confirmed by the UV-vis spectra and PL spectra shown in Fig. S6.†

We can conclude that a sequential crystallization of the donor and acceptor in a PBDB-T/ITIC film could be realized by regulating the order of TA and SVA processes: ITIC crystallizes prior to PBDB-T when the blend film (film-I) was first treated by

SVA and then by TA (TSA-I). In contrast, when the blend film (film-II) was treated with TA before SVA (TSA-II), PBDB-T would crystalize first. The film morphology after TA treatment at 150 °C for 30 min and then SVA for different times is shown in Fig. S7.† The TSA process is shown in Scheme 2.

The crystallization sequence affects the crystallinity of ITIC and film morphology

The UV-vis absorption spectra of the PBDB-T/ITIC pristine film, film-I and film-II are shown in Fig. 2. The blend film shows a narrow response from 450 nm to 760 nm due to the partially overlapped spectra between PBDB-T and ITIC. As shown in Fig. S6(A) and (B),† 450–700 nm is mainly covered by PBDB-T absorption and 500–760 nm is highly absorbed by ITIC. The peaks centered at ca. 635 nm and ca. 700 nm are attributed to the ordered aggregation of PBDB-T and the crystallized ITIC (Fig. 2), respectively. Compared with the pristine film, both film-I and film-II show stronger absorption around ca. 635 nm, which indicated an enhanced crystallinity of PBDB-T in these two films. Whereas, only film-I shows an obvious increased absorption at ca. 700 nm, indicating the crystallinity of ITIC could be improved during the TSA-I process rather than the TSA-II process. The changed crystallinity was also confirmed by photoluminescence (PL) spectroscopy. According to the PL spectra of the neat films (Fig. S6C and D†), it is clear that the peaks centered at ca. 690 nm and ca. 760 nm are the signals of PBDB-T and ITIC, respectively. As shown in Fig. 2(B), after the TSA-I or TSA-II process, the emission intensity from PBDB-T was increased for both film-I and film-II, which is in contrast to the ITIC case where only the enhancement of the emission intensity of film-I was observed. All these data demonstrate that the prior crystallization of ITIC to PBDB-T can improve the crystallinity of ITIC.

GIWAXS was employed to further characterize the texture of the blend films as shown in Fig. 3. For the PBDB-T/ITIC pristine
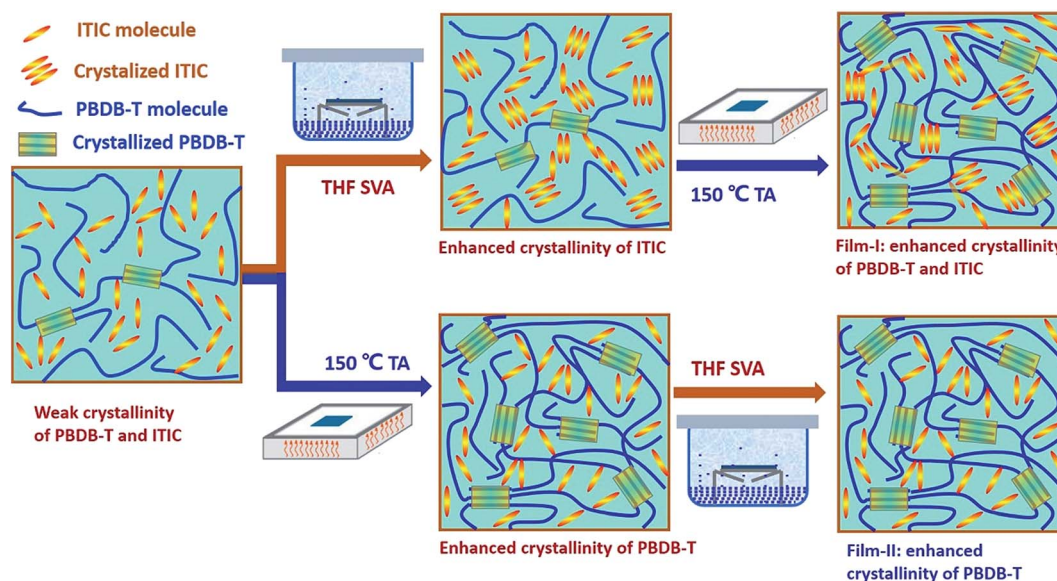
Scheme 2   ITIC and PBDB-T crystallization during the different sequences of TA and SVA treatments.
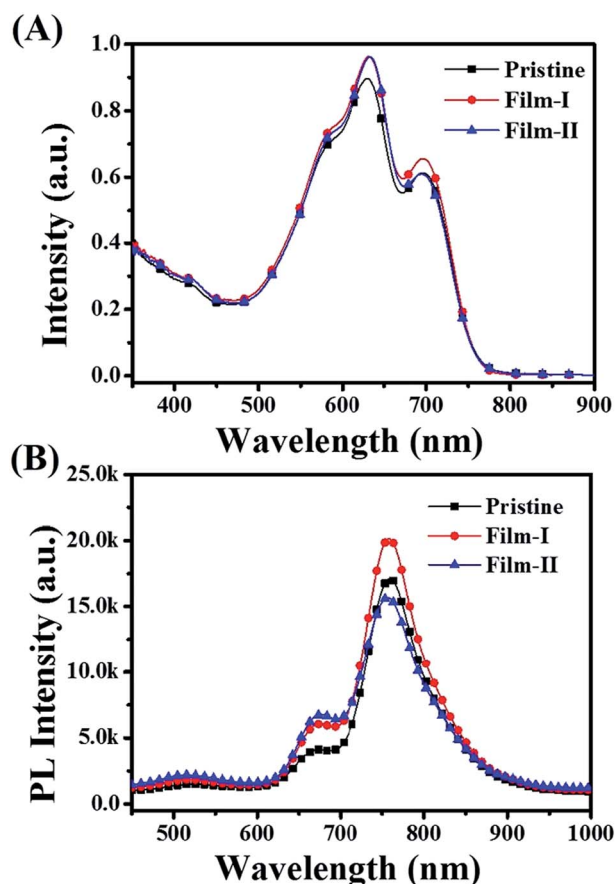
15614 | J. Mater. Chem. A, 2018, 6, 15610–15620

This journal is © The Royal Society of Chemistry 2018

Fig. 2 The UV-vis absorption spectra (A) and the PL spectra (B) of the PBDB-T/ITIC pristine film, film-I and film-II.

film, GIWAXS (Fig. 3(A)) only shows a weak diffraction pattern at 3.2 nm^{-1}, which was attributed to the (100) lamellar peak of PBDB-T, while the diffraction pattern of ITIC was not observed. This observation indicates a low crystallinity PBDB-T (the intensity of peak is only about 100) and amorphous ITIC in the PBDB-T/ITIC blend film. From the GIWAXS patterns of film-I and film-II (Fig. 3(B) and (C)), similar (100) diffraction features of PBDB-T were found with identical peak intensity. This peak intensity is much stronger than the one of the pristine film suggesting higher crystallinity. However, the diffraction signals of ITIC vary with the processing condition: film-I has distinct diffraction signals at 3.5 and 4.2 nm^{-1}, corresponding to the crystallization of ITIC. Whereas, the corresponding signal was almost absent in film-II (for a clear comparison, the corresponding 1D profiles are also presented in Fig. 3(D)). This phenomenon suggests that the crystallinity of PBDB-T could be improved during both TSA-I and TSA-II processes, while the crystallization of ITIC depends on the crystallization sequence, *i.e.*, the prior crystallization of ITIC to PBDB-T, is a key premise to the enhanced crystallinity of ITIC.

The asymmetry of the molecule structure for the blend system exists due to the large difference of molecular weights between PBDB-T and ITIC, PBDB-T would therefore confine the molecular diffusion of ITIC. In the pristine film, the crystallinity of PBDB-T and ITIC is low due to the interference between them. As a result, the crystalline network of PBDB-T has not yet formed. During the TSA-I process, when the film was first treated by SVA, the ITIC molecules could diffuse freely, which results in ITIC nucleation and crystallization. Then, when the film was treated by TA, the strong inter-chain interaction, *i.e.* π–
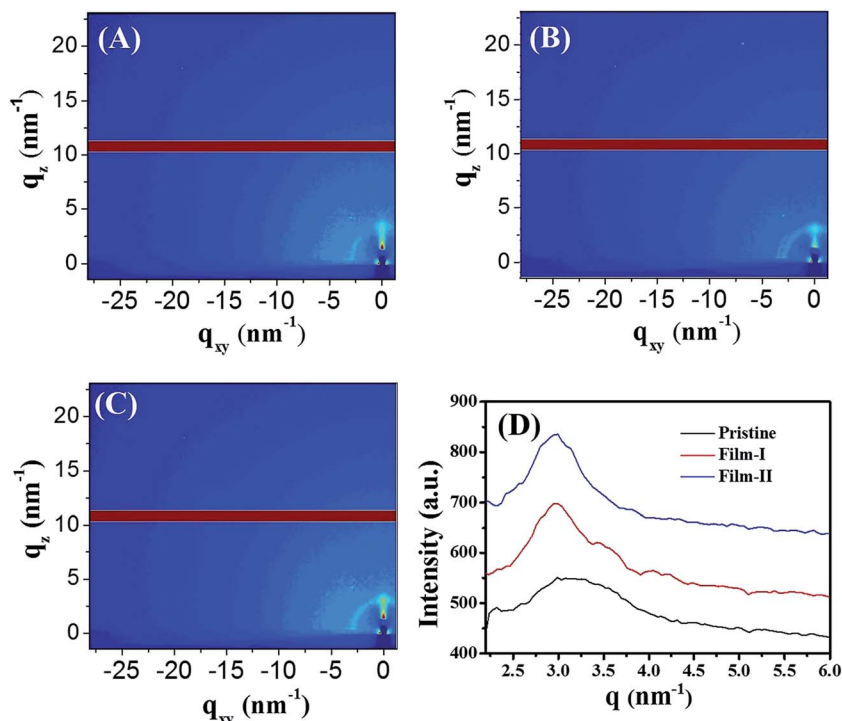

Fig. 3 The GIWAXS diffraction profiles of the PBDB-T/ITIC blend film, pristine film (A), film-I (B), film-II (C) and the intensity *vs. q* for the PBDB-T/ITIC blend film without annealing, film-I and film-II (D).

π interaction, would promote the PBDB-T chains to self-organize. As a result, the crystallinity of both PBDB-T and ITIC was enhanced. The situation is different in the TSA-II process. When the film was first treated by TA, the crystallization of PBDB-T occurred, which induced the formation of a complete crystalline network of PBDB-T. However, when the film was treated by SVA, the diffusion of ITIC was inhibited by the crystalline network of PBDB-T, thus leading to a low crystallinity of ITIC. Hence, it is important to regulate the crystallization sequence to obtain a highly crystalline film.

In addition to the crystallinity, the phase separation structure was also affected by the crystallization sequence. As we know, one primary requirement to construct an interpenetrating network is the formation of continuous pathways with appropriate crystallinity of both the donor and acceptor in BHJ OSCs. AFM images were employed to confirm the formation of an interpenetrating network, as shown in Fig. 4. For the pristine film (Fig. 4(A) and (a)), the film shows a poor phase separation structure with an obscure interphase boundary, which is mainly caused by the inclosure of ITIC in the PBDB-T rich domains. As a result, the continuous pathways for holes and electrons is defective due to the weak crystallization of both PBDB-T and ITIC. However, film-I with an interpenetrating network shows a clear interphase boundary and proper domain size as shown in Fig. 4(B) and (b). This is because the SVA process facilitates the crystallization of ITIC, which makes ITIC form continuous pathways for electron transport. Furthermore, the crystallinity of PBDB-T was also enhanced, thus the

formation of continuous pathways for holes could also be achieved. For film-II, the definition of the phase interface is intermediate between the pristine film and film-I, as shown in Fig. 2 (C) and (c). This is because only the crystallinity of PBDB-T was enhanced, but the crystallization of ITIC was inhibited due to the confinement of the PBDB-T crystalline network. As a result, the ITIC cannot form continuous pathways for electron transport.

The charge-carrier mobility was characterized by using the space-charge-limited current (SCLC) method (as shown in Fig. 5). The hole-only and electron-only device structures are ITO/PEDOT:PSS/active layer/MoO₃/AL and ZnO/active layer/PFNBr/Al, respectively. The carrier mobilities are summarized in Table 1. The pristine film shows a relatively low hole mobility (μ_h) and electron mobility (μ_e) of 1.16×10^{-4} and 1.33×10^{-5} cm² V⁻¹ s⁻¹, respectively. The low mobilities indicate an absence of continuous rich domains of PBDB-T and ITIC for both electron and hole transport within the film. In contrast, the μ_h of film-I increases to 5.04×10^{-4} cm² V⁻¹ s⁻¹ and μ_e increases to 3.20×10^{-4} cm² V⁻¹ s⁻¹ with almost 5 times and 24 times enhancement, respectively. Surprisingly, the transport of holes and electrons became more balanced ($\mu_h/\mu_e = 1.58$) than the pristine film ($\mu_h/\mu_e = 8.72$). The significantly enhanced and balanced hole and electron mobilities indicate the formation of an interpenetrating network, which should be ascribed to the enhanced crystallinity of both the donor and acceptor. Film-II exhibits a μ_h of 4.62×10^{-4} cm² V⁻¹ s⁻¹ as high as that for film-I and a quite low μ_e of only 1.68×10^{-5} cm² V⁻¹ s⁻¹. The
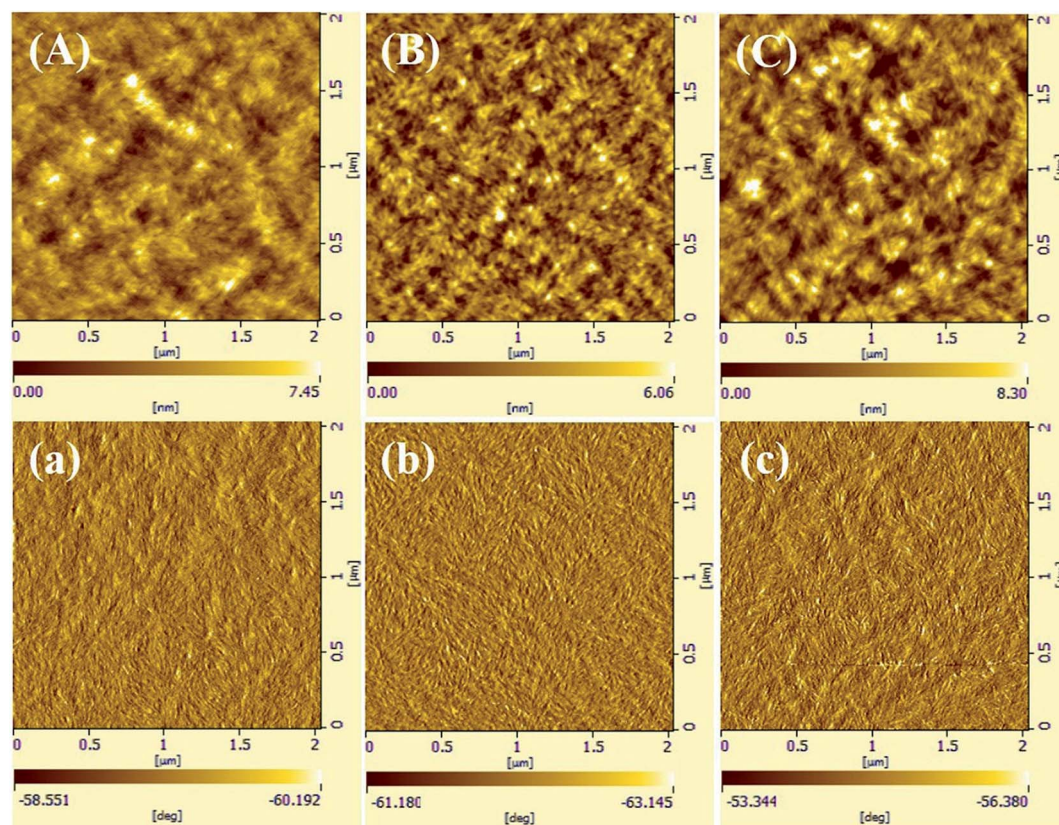

Fig. 4 The height and phase AFM images of the pristine film (A) and (a), film-I (B) and (b), film-II (C) and (c).

15616 | J. Mater. Chem. A, 2018, 6, 15610–15620

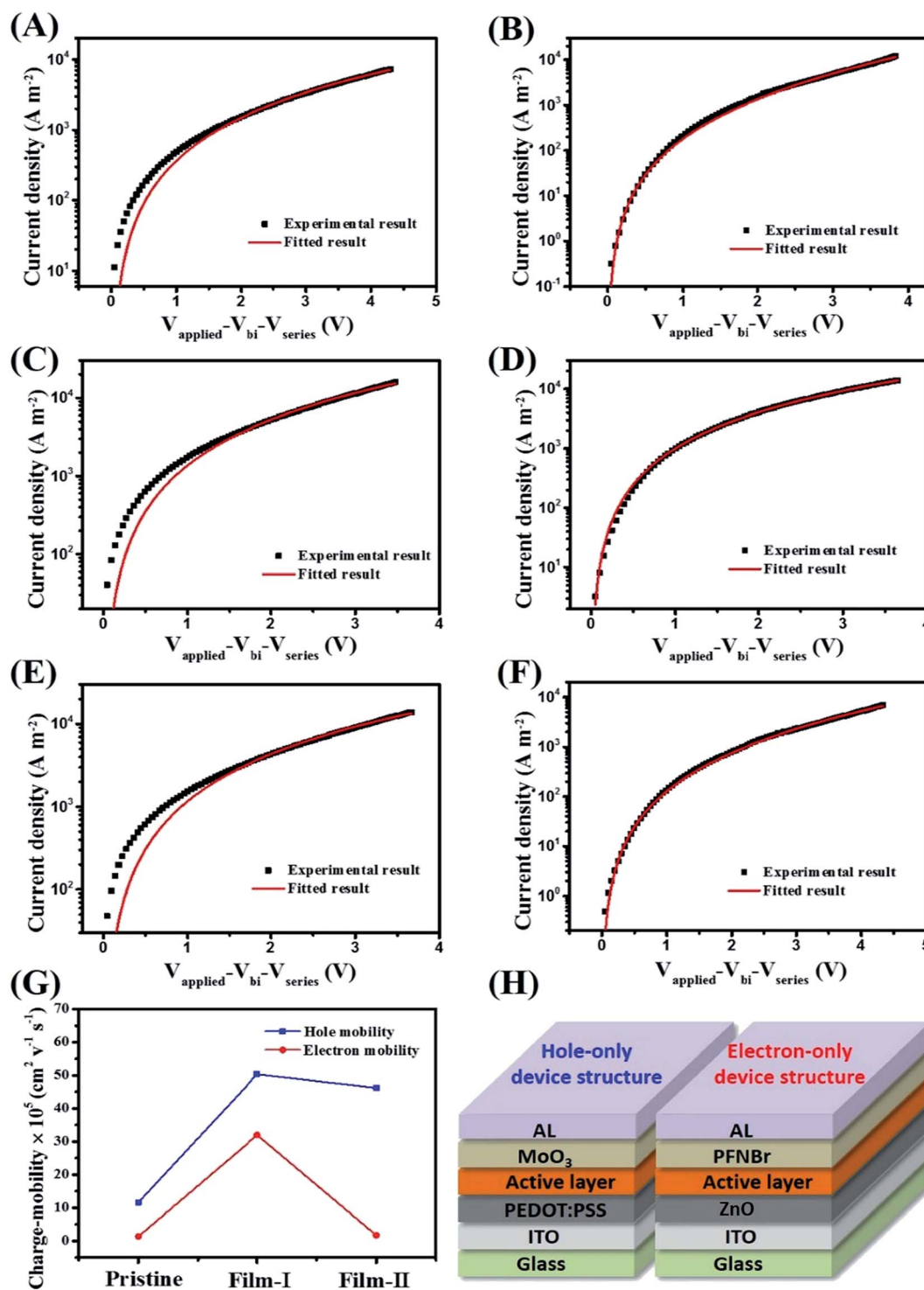This journal is © The Royal Society of Chemistry 2018

Fig. 5 Space-charge-limited $J-V$ characteristics in the dark for hole-only devices of (A) the pristine PBDB-T/ITIC blend film, film-I (C), film-II (E). Space-charge-limited $J-V$ characteristics in the dark for electron-only devices of (B) the pristine PBDB-T/ITIC blend film, film-I (D), film-II (F). The summarization of hole and electron mobilities (G). The structure of hole only and electron only devices (H).

big difference between the hole and electron mobilities is believed to originate from the enhanced crystallinity of PBDB-T but poor crystallinity of ITIC during TSA-II. As a result, only the PBDB-T formed continuous pathways for hole transport, which leads to unbalanced charge transport ($\mu_h/\mu_e = 27.50$).

The relationship between morphology and device performance

In order to explore the influence of crystallization sequence on the photovoltaic performance, solar cells with the ITO/ZnO/PBDB-T:ITIC/MoO$_3$/Al structure were fabricated and characterized. The

This journal is © The Royal Society of Chemistry 2018

J. Mater. Chem. A, 2018, 6, 15610–15620 | 15617

Table 1 The carrier mobilities of the pristine film, film-I and film-II

	Hole mobility ($cm^2\ V^{-1}\ s^{-1}$)	Electron mobility ($cm^2\ V^{-1}\ s^{-1}$)	μ_h/μ_e
Pristine	1.16×10^{-4}	1.33×10^{-5}	8.72
Film-I	5.04×10^{-4}	3.20×10^{-4}	1.58
Film-II	4.62×10^{-4}	1.68×10^{-5}	27.50

photovoltaic parameters of the PBDB-T/ITIC devices without annealing (pristine device) and with TSA-I (device-I) and TSA-II (device-II) are summarized in Table 2, and the corresponding current density voltage (J–V) curves are shown in Fig. 6. The pristine device shows a low short-circuit current density (J_{SC} = 14.30 mA cm^{-2}) and fill factor (FF = 0.63), and the power conversion efficiency (PCE) is only 8.02%. Surprisingly, the J_{SC} and FF increased to 16.73 mA cm^{-2} and 0.74 after TSA-I treatment, respectively. Consequently, the PCE reached to 10.95%. The high J_{SC} and FF should be ascribed to the improved crystallinity of both PBDB-T and ITIC, which promotes the formation of continuous charge transport pathways and diminishes charge recombination. Although the TSA-II treatment also has a positive effect on the device performance, its performance is lower than the device using TSA-I treatment (10.01% vs. 10.95%). The lower PCE mainly originates from the relatively lower FF (0.69 vs. 0.73), while the J_{SC} and V_{OC} remain largely unchanged. The low FF must originate from the poor crystallinity of ITIC and low phase purity, resulting in non-balanced charge transport and bimolecular recombination. The device performance of the PBDB-T/ITIC blend film SVA treated for different times is listed in Table S8.† The device performance of the PBDB-T/ITIC blend film TA treated at 150 °C for 30 min and then SVA treated for different times is listed in Table S9.†

In order to understand the underlying mechanisms governing the differences of device performances, the external quantum efficiency (EQE) spectra are shown in Fig. 6(B). Compared with the pristine device, the EQE spectra of device-I and device-II show obvious improvements in the whole range of the spectrum. The improvements should be ascribed to the enhanced crystallinity, which facilitated the photo absorption and charge transport. In addition, we also compared the EQE spectrum of device-I with the one of device-II in detail, from which a prominent improvement can be observed in the wavelength ranging from 600 nm to 750 nm. It is obvious that the photoabsorption in this range mainly originated from ITIC. As a result, the improvement of the EQE spectrum of device-I should be attributed to the enhanced crystallinity of ITIC.

Table 2 The photovoltaic parameters of the PBDB-T/ITIC blend film processed with different post annealing orders

	V_{OC} (V)	J_{SC} (mA cm^{-2})	FF	Average PCE (%)	Best PCE (%)
Pristine	0.89	14.75	0.62	8.00	8.14
Device-I	0.90	16.73	0.73	10.82	10.95
Device-II	0.89	16.31	0.69	9.87	10.01
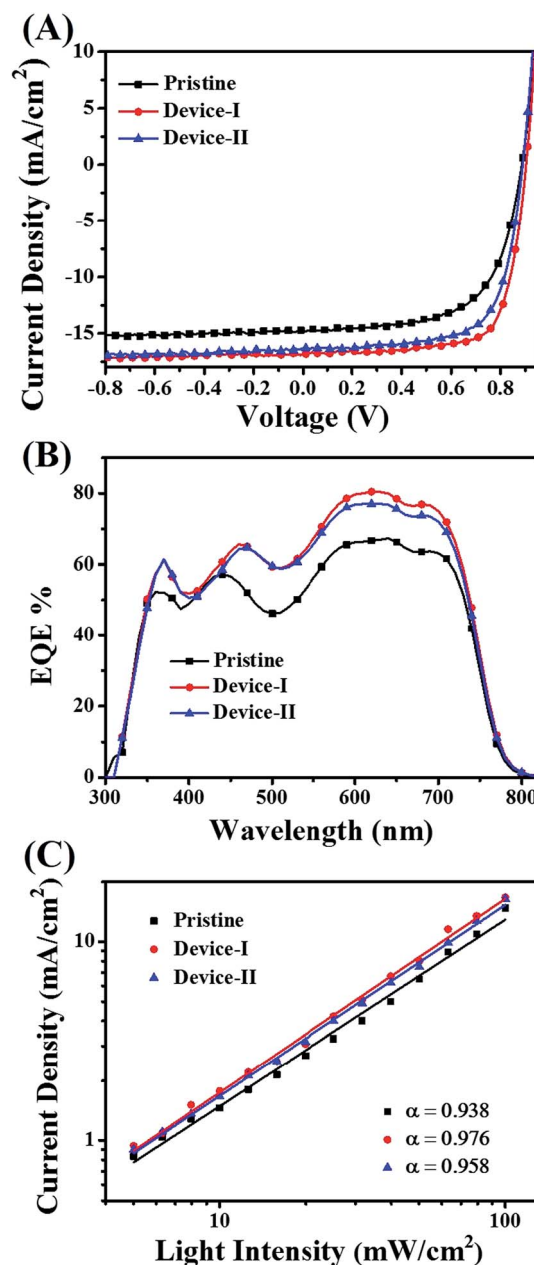
Fig. 6 J–V curves (A), EQE spectra (B), and dependence of the open-circuit voltage on light intensity (C) for devices based on the pristine blend film, film-I and film-II.

The important reason for the improvement of FF is the suppressed bimolecular recombination. The light-intensity dependencies of device performances were studied to identify the charge recombination origin in the devices. The relationship between J_{SC} and light intensity follows the relation $J_{SC} \propto P^{\alpha}$, where P is the light intensity and α is the exponential factor.[36,37] The factor α should be 1 if there is no bimolecular recombination and it is smaller than 1 for the devices with the bimolecular charge recombination.[38,39] As shown in Fig. 6(C), the data are plotted on a log–log scale, and α in the devices was calculated to be 0.93, 0.97 and 0.95 for the pristine device, device-I and device-II, respectively. This indicates that

bimolecular recombination was minimized in device-I. After the TSA-I treatment, the crystallinity of both PBDB-T and ITIC were enhanced, thus forming an interpenetrating network, leading to a balanced charge transport ($\mu_h/\mu_e = 1.57$). In addition, the phase purity was increased as well, which is beneficial for the charge transport. As a result, the bimolecular recombination was suppressed, which agrees well with the remarkable increase in FF.

Conclusion

In summary, we investigated the effect of crystallization sequence on the crystallinity of the polymer donor and SMAs in the strong crystalline polymer donor/weak crystalline SMA blend system. We changed the crystallizing sequence of ITIC and PBDB-T through changing the TA and SVA order, because the TA treatment can selectively improve the crystallinity of PBDB-T at appropriate temperature and THF SVA can only improve the crystallinity of ITIC due to the selective solubility. We found that the prior crystallization of highly crystalline PBDB-T will confine the diffusion of ITIC molecules and inhibit the crystallization of ITIC, leading to poor crystallization of ITIC. In contrast, the prior crystallization of ITIC can avoid the confinement of the PBDB-T crystallized network, improving the crystallinity of ITIC. The enhanced crystallinity of ITIC increased electron mobility from 1.33×10^{-5} to 3.20×10^{-4} cm^2 V^{-1} s^{-1} and reduced the bimolecular recombination. As a result, the device performance is improved from 8.02% to 10.95%. This work demonstrates the importance of the crystallinity of SMAs and points out a way that manipulation of the crystallizing sequence of the donor and acceptor may be key to further boost the efficiency of polymer/SMA solar cells.

Conflicts of interest

There are no conflicts of interest to declare.

Acknowledgements

References

1 B. C. Thompson and J. M. J. Frechet, *Angew. Chem., Int. Ed.*, 2008, **47**, 58–77.

2 A. J. Heeger, *Adv. Mater.*, 2014, **26**, 10–27.

3 H. K. H. Lee, A. M. Telford, J. A. Röhr, M. F. Wyatt, B. Rice, J. Wu, A. de Castro Maciel, S. M. Tuladhar, E. Speller, J. McGettrick, J. R. Searle, S. Pont, T. Watson, T. Kirchartz, J. R. Durrant, W. C. Tsoi, J. Nelson and Z. Li, *Energy Environ. Sci.*, 2018, **11**, 417–428.

4 Y. Cui, H. Yao, C. Yang, S. Zhang and J. Hou, *Acta Polym. Sin.*, 2018, **2**, 223–230.

5 Z. Zhang, S. Zhangm, Z. Liu, Y. Li, C.-Z. Li and H. Chen, *Acta Phys.-Chim. Sin.*, 2018, **34**, 0001–0009.

6 X. Li, J. Yao, I. Angunawela, C. Sun, L. Xue, A. Liebman-Pelaez, C. Zhu, C. Yang, Z.-G. Zhang, H. Ade and Y. Li, *Adv. Energy Mater.*, 2018, 1800815.

7 S. Li, L. Ye, W. Zhao, H. Yan, B. Yang, D. Liu, W. Li, H. Ade and J. Hou, *J. Am. Chem. Soc.*, 2018, **140**, 7159–7167.

8 Z. Xiao, X. Jia and L. Ding, *Sci. Bull.*, 2017, **62**, 1562–1564.

9 H. Zhang, H. Yao, J. Hou, J. Zhu, J. Zhang, W. Li, R. Yu, B. Gao, S. Zhang and J. Hou, *Adv. Mater.*, 2018, e1800613, DOI: 10.1002/adma.201800613.

10 L. M. Chen, Z. R. Hong, G. Li and Y. Yang, *Adv. Mater.*, 2009, **21**, 1434–1449.

11 F. Zhao, C. Wang and X. Zhan, *Adv. Energy Mater.*, 2018, 1703147, DOI: 10.1002/aenm.201703147.

12 S. Nilsson, A. Bernasik, A. Budkowski and E. Moons, *Macromolecules*, 2007, **40**, 8291–8301.

13 W. Ma, J. R. Tumbleston, L. Ye, C. Wang, J. Hou and H. Ade, *Adv. Mater.*, 2014, **26**, 4234–4241.

14 I. A. Howard, R. Mauer, M. Meister and F. Laquai, *J. Am. Chem. Soc.*, 2010, **132**, 14866–14876.

15 X. Yang, J. Loos, S. C. Veenstra, W. J. H. Verhees, M. M. Wienk, J. M. Kroon, M. A. J. Michels and R. A. J. Janssen, *Nano Lett.*, 2005, **5**, 579–583.

16 L. Ye, W. Zhao, S. Li, S. Mukherjee, J. H. Carpenter, O. Awartani, X. Jiao, J. Hou and H. Ade, *Adv. Energy Mater.*, 2017, **7**, 1602000.

17 S. Li, L. Ye, W. Zhao, S. Zhang, H. Ade and J. Hou, *Adv. Energy Mater.*, 2017, **7**, 1700183.

18 H. Hu, K. Jiang, P. C. Y. Chow, L. Ye, G. Zhang, Z. Li, J. H. Carpenter, H. Ade and H. Yan, *Adv. Energy Mater.*, 2018, **8**, 1701674.

19 H. Tanaka, *J. Phys.: Condens. Matter*, 2000, **12**, R207–R264.

20 Z. He, W. Shi, F. Chen, W. Liu, Y. Liang and C. C. Han, *Macromolecules*, 2014, **47**, 1741–1748.

21 S. Holliday, R. S. Ashraf, A. Wadsworth, D. Baran, S. A. Yousaf, C. B. Nielsen, C. H. Tan, S. D. Dimitrov, Z. Shang, N. Gasparini, M. Alamoudi, F. Laquai, C. J. Brabec, A. Salleo, J. R. Durrant and I. McCulloch, *Nat. Commun.*, 2016, **7**, 11585.

22 F. Zhao, S. Dai, Y. Wu, Q. Zhang, J. Wang, L. Jiang, Q. Ling, Z. Wei, W. Ma, W. You, C. Wang and X. Zhan, *Adv. Mater.*, 2017, **29**, 1700144.

23 W. Li, L. Ye, S. Li, H. Yao, H. Ade and J. Hou, *Adv. Mater.*, 2018, **30**, 1707170.

24 H. Yao, L. Ye, J. Hou, B. Jang, G. Han, Y. Cui, G. M. Su, C. Wang, B. Gao, R. Yu, H. Zhang, Y. Yi, H. Y. Woo, H. Ade and J. Hou, *Adv. Mater.*, 2017, **29**, 1700254.

25 D. Leman, M. A. Kelly, S. Ness, S. Engmann, A. Herzing, C. Snyder, H. W. Ro, R. J. Kline, D. M. DeLongchamp and L. J. Richter, *Macromolecules*, 2015, **48**, 383–392.

26 Q. Liang, J. Han, C. Song, Z. Wang, J. Xin, X. Yu, Z. Xie, W. Ma, J. Liu and Y. Han, *J. Mater. Chem. C*, 2017, **5**, 6842–6851.

This journal is © The Royal Society of Chemistry 2018

J. Mater. Chem. A, 2018, **6**, 15610–15620 | **15619**

27 J. Liu, L. Chen, B. Gao, X. Cao, Y. Han, Z. Xie and L. Wang, *J. Mater. Chem. A*, 2013, **1**, 6216–6225.

28 J. Liu, Q. Liang, H. Wang, M. Li, Y. Han, Z. Xie and L. Wang, *J. Phys. Chem. C*, 2014, **118**, 4585–4595.

29 J. Liu, S. Shao, H. Wang, K. Zhao, L. Xue, X. Gao, Z. Xie and Y. Han, *Org. Electron.*, 2010, **11**, 775–783.

30 J. Han, Q. Liang, Y. Qu, J. Liu and Y. Han, *Acta Phys.-Chim. Sin.*, 2018, **34**, 391–406.

31 Y. Chen, C. Zhan and J. Yao, *Chem.–Asian J.*, 2016, **11**, 2620–2632.

32 L. J. A. Koster, V. D. Mihailetchi, H. Xie and P. W. M. Blom, *Appl. Phys. Lett.*, 2005, **87**, 203502.

33 S. Li, L. Ye, W. Zhao, S. Zhang, S. Mukherjee, H. Ade and J. Hou, *Adv. Mater.*, 2016, **28**, 9423–9429.

34 B. Walker, A. Tamayo, D. T. Duong, X.-D. Dang, C. Kim, J. Granstrom and T.-Q. Nguyen, *Adv. Energy Mater.*, 2011, **1**, 221–229.

35 L. Zhang, B. Lin, B. Hu, X. Xu and W. Ma, *Adv. Mater.*, 2018, **30**, e1800343.

36 A. K. K. Kyaw, D. H. Wang, V. Gupta, W. L. Leong, L. Ke, G. C. Bazan and A. J. Heeger, *ACS Nano*, 2013, **7**, 4569–4577.

37 J. Yuan, Y. Xu, G. Shi, X. Ling, L. Ying, F. Huang, T. H. Lee, H. Y. Woo, J. Y. Kim, Y. Cao and W. Ma, *J. Mater. Chem. A*, 2018, **6**, 10421–10432.

38 G. Ding, J. Yuan, F. Jin, Y. Zhang, L. Han, X. Ling, H. Zhao and W. Ma, *Nano Energy*, 2017, **36**, 356–365.

39 Y. Xu, J. Yuan, J. Sun, Y. Zhang, X. Ling, H. Wu, G. Zhang, J. Chen, Y. Wang and W. Ma, *ACS Appl. Mater. Interfaces*, 2018, **10**, 2776–2784.

15620 | *J. Mater. Chem. A*, 2018, **6**, 15610–15620

This journal is © The Royal Society of Chemistry 2018